Two-dimensional transport model of spin-polarized tunneling in a topological-insulator/tunnel-barrier/ferromagnetic-metal heterostructure

Rik Dey,[*] Leonard F. Register, and Sanjay K. Banerjee

Microelectronics Research Center, The University of Texas at Austin, Austin, Texas 78758, USA

Spin-polarized electrons injected from a ferromagnet (FM) onto the surface of a topological insulator (TI) tend to produce a charge current transverse to the direction of the spin polarization because of the spin-momentum helical locking of the TI surface states. The charge current can be measured as an open-circuit voltage that will change in sign if the magnetization direction of the FM is reversed. Here, we model the two-dimensional transport on the TI surface coupled to a FM through a tunnel barrier (TB). The transport equations are solved analytically for two different boundary conditions on the TI surface, and the effectiveness of the TI-TB-FM junction for determining such voltage change upon FM magnetization reversal has been derived for different device dimensions. Such measurement can be used to study the spin-momentum helical locking of the TI surface states as well as for reading the FM magnetization direction in memory and logic devices based on TI-TB-FM heterostructures.

I. INTRODUCTION

The spin-momentum locked helical two-dimensional (2D) surface states of a three-dimensional (3D) topological insulator (TI) have opened up many possibilities for spintronics applications due to efficient manipulation of the spin and the charge degree of freedom of electrons by controlling one with the other [1–5]. The charge current carried by the helical 2D surface states of a 3D TI produces a spin polarization on the surface with the spin orientation perpendicular to the current flow [6–13]. The current-induced spin polarization on the TI surface can be measured with a ferromagnet (FM) [14–28] as well as be utilized for switching the FM magnetization direction [29–34]. Alternatively, a spin-polarized current from the FM onto the TI surface will tend to produce a charge current transverse to the direction of the spin polarization, which is known as the inverse Edelstein effect [35–44]. The inverse Edelstein effect can be observed as an open-circuit voltage in ferromagnetic resonance [45–54] or spin-polarized tunneling [38,55] experiments.

Figure 1(a) shows the schematic of such a spin-polarized tunneling experimental set-up used in the literature [38,55] in which FM-tunnel barrier (TB) heterostructures on the TI surface were used. As shown in Fig. 1(a), a current was passed from the FM to the TI surface through the TB and a voltage drop was measured on the TI surface transverse to the FM magnetization direction. Because of the nonzero density-of-state polarization in the FM, the current is spin-polarized with the polarization direction aligned to that of the FM magnetization direction, and the spin-polarized electrons tend to produce a charge current on the TI surface transverse to the FM magnetization direction. The voltage drop between the two ends of the TI surface, as shown in Fig. 1(a), was observed to change in sign with the reversal of the FM magnetization direction. Such a measurement setup was used to study the helical spin-momentum locking of the TI surface states. The measurement set-up shown in Fig. 1(a) also can be used for reading the FM magnetization direction in which the write path and the read path will be different.

In the literature, transport on the TI surface coupled to a FM has been modeled previously, but those models are only one-dimensional (1D) [6–13,38–42]. The geometry of the setup shown in Fig. 1(a) demands a 2D transport analysis on the TI surface. Although we previously derived the 2D transport equations on the TI surface coupled to a FM through TB, to analyze such experiments we solved the transport equations using a quasi-1D approximation in which we assumed that the component of the current density on the TI surface along the transverse direction (the direction in which the open-circuit voltage drop is measured) is zero in the entire region under the FM [43,44]. However, in our prior work, the potential and the component of the current density along the other direction were allowed to vary on the TI surface in both directions. In this article, we solve the full 2D transport equations on the TI surface coupled to the FM with different type of boundary conditions (Neumann and Dirichlet) imposed on the TI surface without the above-mentioned assumption and show conditions for which our previous approximate results are valid. This paper provides a mathematically rigorous justification of the *a priori* assumptions previously made and the conditions for which such assumptions can be used in practice. Furthermore, the exact analytical solutions provided here for the two-dimensional transport problem for different device parameters can be used to model and fitting experimental results.

To model the spin-polarized tunneling in a TI-TB-FM heterostructure shown in Fig. 1(a), we consider the transport in the rectangular region TI surface underneath the FM

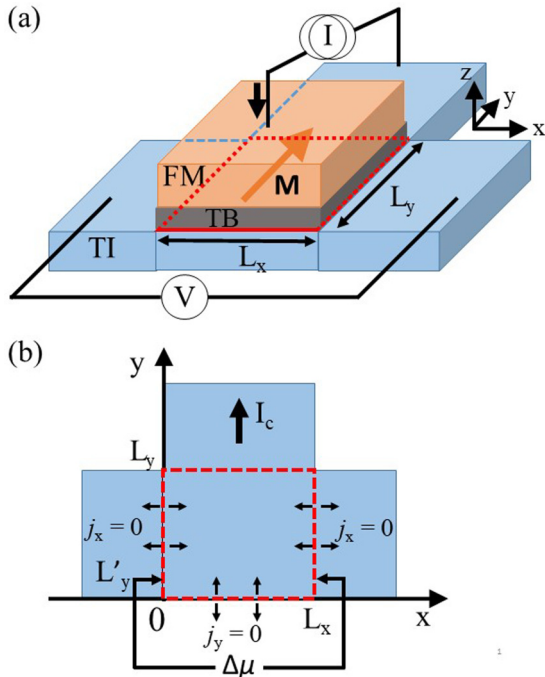*Corresponding author: rikdey@utexas.edu

(a)

(b)

FIG. 1. (a) A schematic of the spin-polarized tunneling experimental set-up for the detection of the inverse Edelstein effect from the topological insulator surface states consisting of topological insulator (TI) - tunnel barrier (TB) - ferromagnetic metal (FM) heterostructure. (b) The transport is modeled in the rectangular region on the TI surface shown by a red dotted line, the total current I_c is flowing out of the boundary $y = L_y$ and electrochemical potential drop $\Delta\mu$ is measured between the boundary $x = 0$ and $x = L_x$ at some $y = L'_y$.

shown by a dotted line in Fig. 1(b), and the boundary conditions are imposed on that rectangular region. We model the voltage measured between two ends on the TI surface, as shown in Fig. 1(a), by the electrochemical potential difference $\Delta\mu$ between the two ends $x = 0$ and $x = L_x$ on the TI surface shown in Fig. 1(b). The total current injected out of the TI surface is I_c, as shown in Fig. 1(b). As net current only can flow out of the TI surface along the $y = L_y$ edge of the rectangle in the inverted T-structure shown in Fig. 1(b), we consider simplified boundary conditions in the rectangular region shown in Fig. 1(b). Open boundary conditions are assumed on the three sides of the rectangular region, which are $j_x(x = 0, y) = 0 \ \forall \ y$, $j_x(x = L_x, y) = 0 \ \forall \ y$ and $j_y(x, y = 0) = 0 \ \forall \ x$. We solve the transport equations assuming two different cases for the boundary condition on the fourth boundary $y = L_y$ of the rectangle. First, we assume the Neumann boundary condition that a uniform surface current density is extracted out of the TI surface across the $y = L_y$ boundary, i.e., $j_y(x, y = L_y) = I_c/L_x \ \forall \ x$. Next, we assume the Dirichlet boundary condition that a uniform electrochemical potential is applied to that boundary on the TI surface such that there is a fixed electrochemical potential difference μ_0 between the FM electrochemical potential μ_c and the $y = L_y$ boundary, i.e., $\mu(x, y = L_y) = \mu_c - \mu_0 \ \forall \ x$. In the case of the Dirichlet boundary condition, the total current out of that fourth boundary is given by $I_c = \int dx \, j_y(x, y = L_y)$. Under

these assumptions, we have neglected any complicated current path outside the rectangular region on the TI surface. In our model, the underlying physics of the spin-polarized tunneling measurement on the TI surface remains the same, and the results derived here should not differ much from that with the actual boundary conditions in the experiment.

II. THEORETICAL MODELING

A. The transport equations

We model diffusive transport on the TI surface by considering spin-independent impurity scattering on the TI surface and by considering spin-conserving momentum-randomizing tunneling of electrons back and forth between the TI and the FM which serve to reduce mobility on the TI surface in addition to providing charge injection into the TI from the FM. In steady state, the modified continuity equation for the charge density on the TI surface is given by [8,43]

$$\nabla_{\mathbf{R}} \cdot \mathbf{J} = -\gamma N_+ n + \gamma N n_+ + \frac{\gamma N_-}{v_F} \mathbf{J} \cdot (\hat{\mathbf{m}} \times \hat{\mathbf{z}}), \quad (1)$$

where n is the charge density and $\mathbf{J}$ is the charge current density on the TI surface, the $n_\pm$ are the charge and spin densities in the FM, respectively, defined as $n_\pm = n_\uparrow \pm n_\downarrow$ where the $n_{\uparrow,\downarrow}$ are the density of the spin up and spin down electrons in the FM, N is the density of states of the TI surface states at the Fermi energy, $N_\pm = N_\uparrow \pm N_\downarrow$ where $N_{\uparrow,\downarrow}$ is the density of spin up and spin down states in the FM at the Fermi energy, v_F is the Fermi velocity of the TI surface states, $\hat{\mathbf{m}}$ is the FM magnetization direction, and γ is proportional to the tunneling rate of electrons between the FM spin states and the TI surface states. In steady state, the modified diffusion equation for the charge current density on the TI surface is given by [8,43]

$$\mathbf{J} = \frac{1}{(1 + \xi)} \left[-D \nabla_{\mathbf{R}} n + \frac{\gamma v_F \tau_{tr}}{2} (N_- n - N n_-)(\hat{\mathbf{m}} \times \hat{\mathbf{z}}) \right]. \quad (2)$$

Here, τ_{tr} is the transport relaxation time on the pristine TI surface without any tunneling from the FM, $D = v_F^2 \tau_{tr}/2$ is the diffusion constant on the pristine TI surface without any tunneling. The dimensionless parameter $\xi = \gamma N_+ \tau_{tr}$ denotes the normalized tunneling rate of electrons between the TI and the FM (normalized to the transport relaxation rate of electrons on the TI surface), where γN_+ is the effective interface tunneling rate between the TI and the FM.

We define the electrochemical potential μ on the TI surface by $n = e^2 N \mu$, and the electrochemical potential $\mu_{\uparrow,\downarrow}$ for the majority and minority electrons in the FM as $\mu_{\uparrow,\downarrow}$ by $n_{\uparrow,\downarrow} = e^2 N_{\uparrow,\downarrow} \mu_{\uparrow,\downarrow}$. For the device geometry shown in Fig. 1(a), for a spatially constant charge electrochemical potential μ_c applied in the FM, the electrochemical potentials for both the majority and minority electrons in the FM become μ_c, i.e., $\mu_\uparrow = \mu_\downarrow = \mu_c$. Then, from Eqs. (1) and (2), we obtain the following equation for the electrochemical potential μ on the TI surface,

$$\partial_x^2 \mu + \partial_y^2 \mu - 2b_0 m_y \partial_x \mu + 2b_0 m_x \partial_y \mu$$
$$+ \left[b_0^2 (m_x^2 + m_y^2) - c_0^2 \right] (\mu - \mu_c) = 0, \quad (3)$$

where $b_0 = \xi\eta/l_{\rm tr}$, $\eta = \frac{N_-}{N_+}$ is the density of state polarization of the FM, $l_{\rm tr} = v_{\rm F}\tau_{\rm tr}$ is the transport relaxation length on the pristine TI surface, and $c_0 = \sqrt{2\xi(1+\xi)}/l_{\rm tr}$. On the pristine TI surface, the transport relaxation time $\tau_{\rm tr}$ is related to the scattering time $\tau_{\rm p}$ by $\tau_{\rm tr} = 2\tau_{\rm p}$, due to the requirements of spin conservation which prevent direct backscattering, and the mean free path $l_{\rm m}$ is given by $l_{\rm m} = v_{\rm F}\tau_{\rm p}$. The current density $\mathbf{J}$ on the TI surface can be written as $\mathbf{J} = j_x\hat{x} + j_y\hat{y}$, where the x and y components of the current density are given by

$$j_x = -\sigma'[\partial_x\mu - b_0 m_y(\mu - \mu_{\rm c})], \tag{4a}$$

$$j_y = -\sigma'[\partial_y\mu + b_0 m_x(\mu - \mu_{\rm c})]. \tag{4b}$$

Here, $\sigma' = \sigma/(1+\xi)$ is the modified conductivity of the TI surface due to tunneling from the FM, and $\sigma = e^2 ND$ is the conductivity of the pristine TI surface without tunneling. The conductivity of the TI surface underneath the FM is modified because the spin conserving but otherwise momentum randomizing tunneling back and forth between the TI and the FM provides momentum relaxing scattering apart from the scattering from impurities on the TI surface and from the TI-FM interface imperfections. In our previous work [43], the derivations of Eqs. (1)–(4) are provided in detail.

B. A solution method for the transport equations

To solve Eq. (3), we make the following substitution: $\mu(x,y) = \mu_{\rm c} + \tilde{\mu}(x,y)e^{b_0(m_y x - m_x y)}$. Since $\mu_{\rm c}$ is spatially constant, i.e., $\partial_x\mu_{\rm c} = 0 = \partial_y\mu_{\rm c}$, from Eq. (3), we obtain

$$\partial_x^2\tilde{\mu} + \partial_y^2\tilde{\mu} - c_0^2\tilde{\mu} = 0. \tag{5}$$

After the same substitution, from Eq. (4), we obtain

$$j_x = -\sigma' e^{b_0(m_y x - m_x y)}\partial_x\tilde{\mu}, \tag{6a}$$

$$j_y = -\sigma' e^{b_0(m_y x - m_x y)}\partial_y\tilde{\mu}. \tag{6b}$$

Equation (5) is the modified Helmholtz equation, which is a second-order homogeneous elliptic partial differential equation. We solve Eq. (5) by the technique of separation of variables and series solution with appropriate boundary conditions on the boundary of the TI surface of rectangular shape $[0, L_x] \times [0, L_y]$, as shown in Fig 1(b).

After separation of variables, i.e., setting $\tilde{\mu}(x,y) = \tilde{\mu}_X(x)\tilde{\mu}_Y(y)$ in Eq. (5), we obtain

$$\frac{d_x^2\tilde{\mu}_X}{\tilde{\mu}_X} + \frac{d_y^2\tilde{\mu}_Y}{\tilde{\mu}_Y} = c_0^2. \tag{7}$$

From Eq. (7), we have $d_x^2\tilde{\mu}_X = c_X^2\tilde{\mu}_X$ and $d_y^2\tilde{\mu}_Y = c_Y^2\tilde{\mu}_Y$, where c_X, c_Y can have real and imaginary parts and satisfy the constraint $c_X^2 + c_Y^2 = c_0^2$. We obtain the general solutions as $\tilde{\mu}_X(x) = A_1 e^{c_X x} + A_2 e^{-c_X x}$ if $c_X \neq 0$, $\tilde{\mu}_X(x) = A_1 + A_2 x$ if $c_X = 0$, and $\tilde{\mu}_Y(y) = B_1 e^{c_Y y} + B_2 e^{-c_Y y}$ if $c_Y \neq 0$, $\tilde{\mu}_Y(y) = B_1 + B_2 y$ if $c_Y = 0$. Then, from Eq. (6), we have $j_x(x,y) = -\sigma' e(x,y) c_X (A_1 e^{c_X x} - A_2 e^{-c_X x})\tilde{\mu}_Y(y)$ if $c_X \neq 0$, $j_x(x,y) = -\sigma' e(x,y) A_2\tilde{\mu}_Y(y)$ if $c_X = 0$, and $j_y(x,y) = -\sigma' e(x,y) c_Y (B_1 e^{c_Y y} - B_2 e^{-c_Y y})\tilde{\mu}_X(x)$ if $c_Y \neq 0$, $j_y(x,y) = -\sigma' e(x,y) B_2\tilde{\mu}_X(x)$ if $c_Y = 0$, where $e(x,y) = e^{b_0(m_y x - m_x y)}$.

To solve the electrochemical potential μ on the TI surface in our previous work [43,44], we assumed that $j_x = 0$ on the TI surface under the FM region in the device geometry shown in Fig. 1(b). However, $j_x(x,y) = 0 \,\forall\, x, y$ is a strict condition on the current distribution inside the rectangular region on the TI surface. Instead, the current distribution inside the rectangular region should be determined by the other two boundary conditions imposed on the boundaries $y = 0$ and $y = L_y$. Furthermore, we assumed $j_y(x, y = 0) = 0 \,\forall\, x$ on the boundary $y = 0$, and for the boundary $y = L_y$ we took the total current injected out of that boundary as $I_{\rm c}$, i.e., $\int dx\, j_y(x, y = L_y) = I_{\rm c}$. However, the condition $\int dx\, j_y(x, y = L_y) = I_{\rm c}$ is not a boundary condition of the differential equation, Eq. (3). Nevertheless, this condition is physically relevant and was used to obtain the solution of $\mu(x,y)$ with the approximation $j_x = 0$ inside the rectangle. In this work, we solve the two-dimensional transport equation, i.e., Eq. (3) or (5), exactly for two different boundary conditions assumed on the boundary $y = L_y$ of the rectangular region shown in Fig. 1(b) without assuming that the x-component of the current density, j_x, is zero inside the entire rectangular region, although we have taken $j_x = 0$ on the boundary $x = 0$ and $x = L_x$ along with $j_y = 0$ on the boundary $y = 0$. We will discuss the condition for which the prior result is an approximation of the exact results obtained here within these boundary conditions.

We are looking for a nontrivial solution for $\tilde{\mu}(x,y)$ given the boundary condition $j_x(x = 0, y) = 0 = j_x(x = L_x, y)$. If $c_X = 0$, from the boundary conditions we obtain $\tilde{\mu}_X(x)$ to be constant. If $c_X \neq 0$, then the boundary condition $j_x(x = 0, y) = 0$, $\forall\, y$ implies $c_X(A_1 - A_2) = 0$, and the boundary condition $j_x(x = L_x, y) = 0$, $\forall\, y$ implies $c_X A_1(e^{c_X L_x} - e^{-c_X L_x}) = 0$, which implies c_X cannot have real part and must be purely imaginary. We take $c_X = \iota c_n$ and c_n must satisfy $\sin(c_n L_x) = 0$, which gives $c_n = n\pi/L_x$, $c_Y = \sqrt{c_0^2 + c_n^2}$, where n is a nonzero integer (positive or negative). So, $\tilde{\mu}_X(x)$ will be given by $\tilde{\mu}_X(x) = \tilde{A}_n \cos(n\pi/L_x)$, and we can also include the $c_X = 0$ case (i.e., $c_n = 0$ for $n = 0$ and $\tilde{\mu}_X(x) = \tilde{A}_0$). From the boundary condition $j_y(x, y = 0) = 0 \,\forall\, x$, we obtain that $\tilde{\mu}_Y(y)$ must be given by $\tilde{\mu}_Y(y) = \tilde{B}_n \cosh(\sqrt{c_0^2 + n^2\pi^2/L_x^2}\,y)$. Then, the general solution for $\tilde{\mu}(x,y)$ is given by the series

$$\tilde{\mu}(x,y) = \sum_{n=0}^{\infty} \tilde{D}_n \cos\left(\frac{n\pi x}{L_x}\right) \cosh\left(\sqrt{c_0^2 + \frac{n^2\pi^2}{L_x^2}}\,y\right). \tag{8}$$

Here, $\tilde{D}_0 = \tilde{A}_0\tilde{B}_0$, and $\tilde{D}_n = \tilde{A}_n\tilde{B}_n + \tilde{A}_{-n}\tilde{B}_{-n}$ for positive integer $n \neq 0$ [the contributions for positive and negative integers are already added in individual term in Eq. (8)].

In the rest of the article, we only consider FM magnetization in the y direction ($m_x = 0$, $m_y = \pm 1$), as shown in Fig. 1(a). Then, $\mu(x,y)$ on the TI surface is given by

$$\mu = \mu_{\rm c} + e^{b_0 m_y x} \sum_{n=0}^{\infty} \tilde{D}_n \cos\left(\frac{n\pi x}{L_x}\right) \cosh\left(\sqrt{c_0^2 + \frac{n^2\pi^2}{L_x^2}}\,y\right). \tag{9}$$

From Eqs. (6b) and (8), for $m_x = 0$, we have

$$j_x(x, y) = \sigma' e^{b_0 m_y x} \sum_{n=0}^{\infty} \tilde{D}_n \left(\frac{n\pi}{L_x} \right) \sin \left(\frac{n\pi x}{L_x} \right)$$

$$\times \cosh \left(\sqrt{c_0^2 + \frac{n^2 \pi^2}{L_x^2}} y \right), \qquad (10)$$

$$j_y(x, y) = -\sigma' e^{b_0 m_y x} \sum_{n=0}^{\infty} \tilde{D}_n \sqrt{c_0^2 + \frac{n^2 \pi^2}{L_x^2}}$$

$$\times \cos \left(\frac{n\pi x}{L_x} \right) \sinh \left(\sqrt{c_0^2 + \frac{n^2 \pi^2}{L_x^2}} \right). \qquad (11)$$

The unknown coefficients $\tilde{D}_n$ will be determined from the boundary condition for either j_y (Neumann condition) or μ (Dirichlet condition) on the boundary $y = L_y$.

III. RESULTS AND DISCUSSIONS

A. Solution for the Neumann boundary condition

First, we solve the transport problem for the Neumann boundary condition of uniform current density on the boundary $y = L_y$ of the rectangular region on the TI surface shown in Fig. 1(b), i.e., $j_y(x, y = L_y) = I_c/L_x \; \forall \, x \in [0, L_x]$. Using Eq. (11) in the boundary condition $j_y(x, y = L_y) = I_c/L_x \; \forall \, x \in [0, L_x]$, we obtain

$$\sum_{n=0}^{\infty} \tilde{E}_n \cos \left(\frac{n\pi x}{L_x} \right) = -\left(\frac{I_c}{\sigma' L_x} \right) e^{-b_0 m_y x}, \qquad (12)$$

where

$$\tilde{E}_n = \tilde{D}_n \sqrt{c_0^2 + \frac{n^2 \pi^2}{L_x^2}} \sinh \left(\sqrt{c_0^2 + \frac{n^2 \pi^2}{L_x^2}} L_y \right). \qquad (13)$$

The left side of Eq. (12) is a Fourier series representation of the function given on the right side of Eq. (12) in the interval $x \in [0, L_x]$. The coefficient $\tilde{E}_0$ is given by

$$\tilde{E}_0 = -\left(\frac{I_c}{\sigma' L_x} \right) \frac{1}{L_x} \int_0^{L_x} dx \, e^{-b_0 m_y x}$$

$$= -\left(\frac{I_c}{\sigma' L_x} \right) \frac{(1 - e^{-b_0 m_y L_x})}{b_0 m_y L_x}, \qquad (14)$$

and, for $n \neq 0$, the coefficients $\tilde{E}_n$ are given by

$$\tilde{E}_n = -\left(\frac{I_c}{\sigma' L_x} \right) \frac{2}{L_x} \int_0^{L_x} dx \, e^{-b_0 m_y x} \cos \left(\frac{n\pi x}{L_x} \right)$$

$$= -\left(\frac{I_c}{\sigma' L_x} \right) \frac{2 b_0 m_y L_x [1 - (-1)^n e^{-b_0 m_y L_x}]}{(b_0^2 m_y^2 L_x^2 + n^2 \pi^2)}. \qquad (15)$$

The coefficients $\tilde{D}_n$'s are obtained from Eqs. (13)–(15), and the solutions of $\mu(x, y)$ and $j_x(x, y)$ are given by Eqs. (9)–(11) since all the $\tilde{D}_n$'s are known. As shown in Fig. 1(b), the electrochemical potential difference $\Delta\mu(L_y')$ is measured between the two ends $x = 0$ and $x = L_x$ on the TI surface at $y = L_y' (0 < L_y' < L_y)$ given $m_y = \pm 1$, where $\Delta\mu(L_y') = \mu(x = 0, y = L_y') - \mu(x = L_x, y = L_y')$. The formula for

$\Delta\mu(L_y')$ is given in Appendix A, see Eq. (A1). As seen from Eq. (A1), the potential difference $\Delta\mu(L_y')$ depends on the charge current I_c and magnetization direction m_y of the FM, and $\Delta\mu(L_y')$ changes sign if either the charge current direction or the FM magnetization direction is reversed.

If $b_0 L_x = \xi \eta L_x/l_{tr} < 1$, $L_y > L_x$ and $(L_y - L_y') > L_x$, all the terms in Eq. (A1) for $n \geqslant 1$ can be neglected compared to the first term, and $\sinh^2(b_0 L_x/2) \approx b_0^2 L_x^2/4$ can be used in the first term. Then, from Eq. (A1), we obtain

$$\Delta\mu(L_y') = \frac{I_c}{\sigma} \frac{\eta m_y}{2} \frac{l_{tr}}{L_y} \frac{(d_0 L_y/l_{tr}) \cosh(d_0 L_y'/l_{tr})}{\sinh(d_0 L_y/l_{tr})}, \qquad (16)$$

where $d_0 = c_0 l_{tr} = \sqrt{2\xi(1 + \xi)}$. Equation (16) is what we obtained in our prior work with the approximation $j_x = 0$ inside the rectangle [43,44]. The Eq. (16) is an approximate solution when L_x is comparable to l_{tr} (since typically ξ and η are smaller than 1, the condition $b_0 L_x = \xi \eta L_x/l_{tr} < 1$ will be satisfied), L_y is large compared to L_x, and L_y' is closer to the boundary $y = 0$ than the boundary $y = L_y$. In our previous work, we defined a dimensionless parameter χ from $\Delta\mu$ by

$$\Delta\mu = \chi \frac{I_c}{\sigma} \frac{\eta m_y}{2} \frac{l_{tr}}{L_y}. \qquad (17)$$
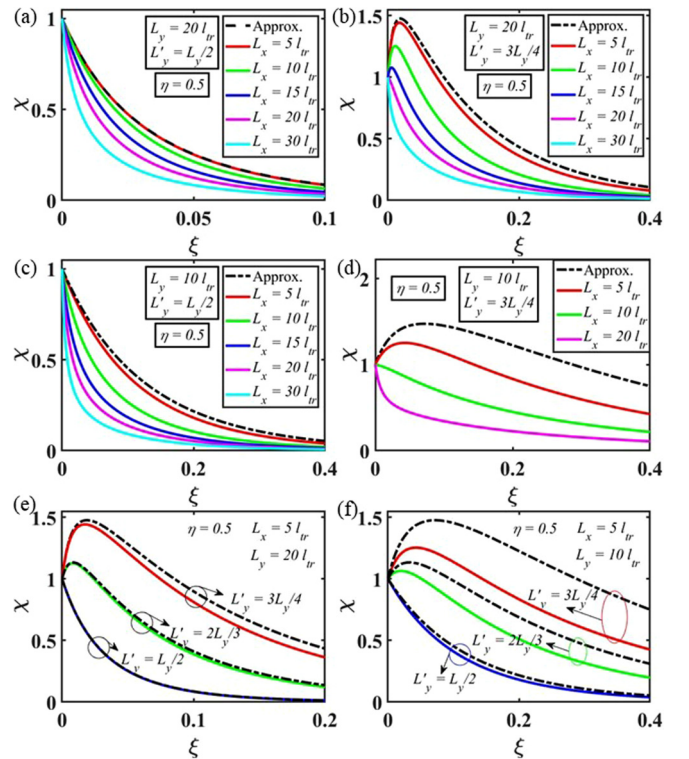

FIG. 2. Variation of χ with ξ calculated for the Neumann boundary condition is compared with the approximate result (dotted line): (a)–(c) for different $L_x/l_{tr} = 5, 10, 15, 20, 30$, and (a) $L_y/l_{tr} = 20$, $L_y' = L_y/2$, (b) $L_y/l_{tr} = 20$, $L_y' = 3L_y/4$, (c) $L_y/l_{tr} = 10$, $L_y' = L_y/2$, and (d) for different $L_x/l_{tr} = 5, 10, 20$, $L_y/l_{tr} = 10$, and $L_y' = 3L_y/4$. The variation of χ with ξ for the approximate result is independent of L_x, but depends on L_y and L_y'. [(e)–(f)] Results for different $L_y'/L_y = 1/2, 2/3, 3/4$, $L_x/l_{tr} = 5$ and (e) $L_y/l_{tr} = 20$, (f) $L_y/l_{tr} = 10$. All results are calculated for $\eta = 0.5$.

For the approximation $j_x = 0$ inside the rectangle, from Eqs. (16) and (17), we obtained

$$\chi = (d_0 L_y / l_{\text{tr}}) \cosh(d_0 L_y' / l_{\text{tr}}) / \sinh(d_0 L_y / l_{\text{tr}}), \quad (18)$$

which is independent of the length L_x. In the general case here, we similarly define $\chi \equiv \Delta G / \Delta G^0$, where the change of conductance $\Delta G = \Delta \mu / I_c$ is obtained from Eq. (A1), and

$$\Delta G^0 = \frac{1}{\sigma} \frac{\eta m_y}{2} \frac{l_{\text{tr}}}{L_y}. \quad (19)$$

We note that in the limit $\xi \to 0$ for the Neumann boundary condition, $\Delta G(\xi \to 0) = \Delta G^0$ from Eq. (A1). The dimensionless parameter χ can be viewed as the effectiveness of the device in the detection of the inverse Edelstein effect from the TI surface states. The variations of χ with ξ obtained from the solution of the Neumann boundary condition are shown in Figs. 2–5 for different values of L_x / l_{tr}, L_y / l_{tr}, L_y' and η.

In Figs. 2(a)–2(d), we show the variation of χ with ξ for different values of L_x / l_{tr} and a given L_y / l_{tr}, L_y' / L_y, and η. The approximate solutions also are plotted in the same figures for comparison. The variation of χ with ξ for the approximate result, i.e., Eq. (18), is independent of L_x but depends on L_y and L_y'. As seen from Figs. 2(a)–2(d), a given L_y / l_{tr}, L_y', η and ξ, the value of χ from the solution of the Neumann boundary condition decreases with increasing L_x / l_{tr} and deviates from the approximate result with increasing L_x / l_{tr}. It is evident from Figs. 2(a)–2(d) that the validity of the approximate result holds for $b_0 L_x < 1$, $L_y > L_x$ and $(L_y - L_y') > L_x$. In Figs. 2(e)–2(f), the variation of χ with ξ is shown for different values of L_y' / L_y and a given L_x / l_{tr}, L_y / l_{tr} and η. Similarly, it is seen from Figs. 2(e)–2(f) that the value of χ for the Neumann boundary condition deviates more from the approximate one
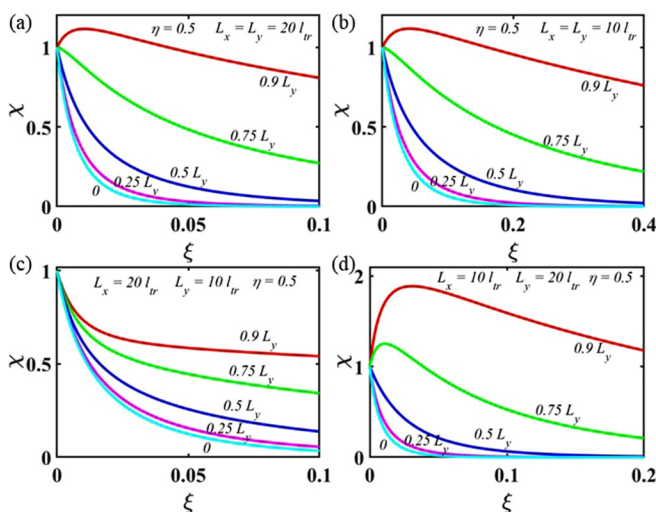

FIG. 4. Variation of χ with ξ for different $L_y / l_{\text{tr}} = 5, 10, 20, 30, 40$, and (a) $L_x / l_{\text{tr}} = 20$, $L_y' = 0$, (b) $L_x / l_{\text{tr}} = 10$, $L_y' = 0$, (c) $L_x / l_{\text{tr}} = 20$, $L_y' / l_{\text{tr}} = 5$, (d) $L_x / l_{\text{tr}} = 10$, $L_y' / l_{\text{tr}} = 5$, (e) $L_x / l_{\text{tr}} = 20$, $L_y' = 0.9L_y$, and (f) $L_x / l_{\text{tr}} = 10$, $L_y' = 0.9L_y$. The results for $L_y = L_y' = 5l_{\text{tr}}$ are not shown for (c) and (d). Since the results are plotted for different L_y's in (e) and (f) keeping $L_y' = 0.9L_y$ the same, the value of L_y' also varies with L_y in (e) and (f). All results are calculated for $\eta = 0.5$.

FIG. 3. Variation of χ with ξ for different $L_y' / L_y = 0.9, 0.75, 0.5, 0.25, 0$, and (a) $L_x / l_{\text{tr}} = L_y / l_{\text{tr}} = 20$, (b) $L_x / l_{\text{tr}} = L_y / l_{\text{tr}} = 10$, (c) $L_x / l_{\text{tr}} = 20$, $L_y / l_{\text{tr}} = 10$, and (d) $L_x / l_{\text{tr}} = 10$, $L_y / l_{\text{tr}} = 20$. All results are calculated for $\eta = 0.5$.

when the conditions $b_0 L_x < 1$, $L_y > L_x$ and $(L_y - L_y') > L_x$ are not satisfied.

In Figs. 3(a)–3(d), we show the variation of χ with ξ for different values of L_y' / L_y and a given L_x / l_{tr}, L_y / l_{tr} and η. As seen from Figs. 3(a)–3(d), a given L_x / l_{tr}, L_y / l_{tr}, η and ξ, the value of χ increases with increasing L_y' / L_y. In Figs. 4(a)–4(d), the variation of χ with ξ are shown for different values of L_y / l_{tr} and a given L_x / l_{tr}, L_y' / l_{tr}, η. It is clear from Figs. 4(a)–4(d) that a given L_x / l_{tr}, L_y' / l_{tr}, η and ξ, the value of χ decreases with increasing L_y / l_{tr}. The experimental quantity of interest is ΔG which is given by $\Delta G = \chi \Delta G^0$. Since ΔG^0 given in Eq. (19) is inversely proportional to L_y / l_{tr}, the value of ΔG decreases further with increasing L_y / l_{tr}. In Figs. 4(e)–4(f), the variation of χ with ξ are shown for different values of L_y / l_{tr} keeping L_y' / L_y the same and a given L_x / l_{tr}, η. However, the change of behavior of χ with ξ is not monotonic with increasing L_y / l_{tr} as compared to Figs. 4(a)–4(d), since the value of L_y' / l_{tr} [the value where ΔG is calculated as shown in Fig. 1(b)] also changes with L_y / l_{tr}. In Figs. 5(a)–5(d), we show the variation of χ with ξ for different values of η and a given L_x / l_{tr}, L_y / l_{tr} and L_y' / L_y. Although the value of χ slightly decreases with decreasing η, the value of ΔG will almost proportionally decrease with decreasing η because ΔG is proportional to ΔG^0 which is proportional to η [Eq. (19)].

FIG. 5. Variation of χ with ξ for different $\eta = 0.99, 0.50, 0.01$ and $L'_y/L_y = 0.9, 0.75$, and (a) $L_x/l_{tr} = L_y/l_{tr} = 20$, (b) $L_x/l_{tr} = L_y/l_{tr} = 10$, (c) $L_x/l_{tr} = 20$, $L_y/l_{tr} = 10$, and (d) $L_x/l_{tr} = 10$, $L_y/l_{tr} = 20$. The results for $\eta = 0.5$ are shown by dotted lines.
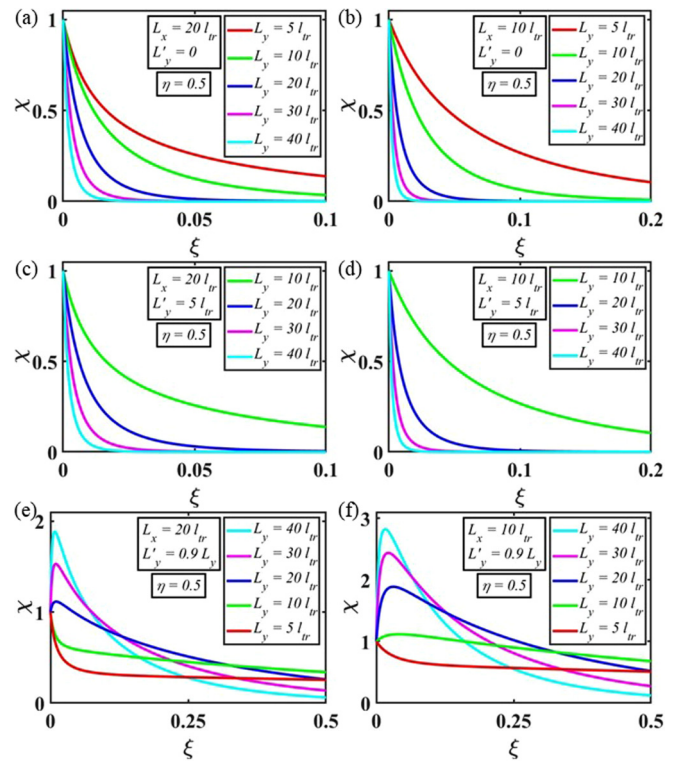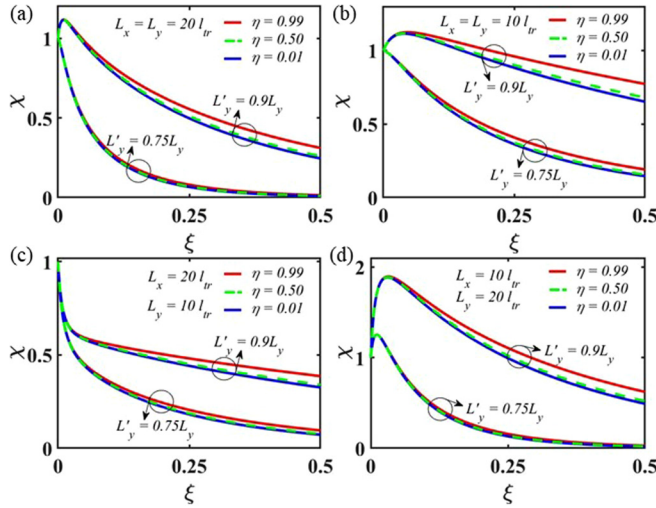
B. Solution for the dirichlet boundary condition

We next solve the transport problem for the Dirichlet boundary condition of uniform electrochemical potential $\mu_c - \mu_0$ applied on the boundary $y = L_y$ of the rectangular region on the TI surface shown in Fig. 1(b), i.e., $\mu(x, y = L_y) - \mu_c = -\mu_0 \; \forall \; x \in [0, L_x]$. Inserting Eq. (9) in the condition $\mu(x, y = L_y) - \mu_c = -\mu_0 \; \forall \; x \in [0, L_x]$, we obtain

$$\sum_{n=0}^{\infty} \tilde{F}_n \cos\left(\frac{n\pi x}{L_x}\right) = -\mu_0 e^{-b_0 m_y x}, \tag{20}$$

where

$$\tilde{F}_n = \tilde{D}_n \cosh\left(\sqrt{c_0^2 + \frac{n^2\pi^2}{L_x^2}} L_y\right). \tag{21}$$

The left side of Eq. (20) is a Fourier series representation of the function given on the right side of Eq. (20) in the interval $x \in [0, L_x]$. The coefficients $\tilde{F}_n$'s are obtained similarly as $\tilde{E}_n$'s in Eq. (14) and (15). The coefficient $\tilde{F}_0$ is given by

$$\tilde{F}_0 = -\mu_0 \frac{1}{L_x} \int_0^{L_x} dx \; e^{-b_0 m_y x} = -\mu_0 \frac{(1 - e^{-b_0 m_y L_x})}{b_0 m_y L_x}, \tag{22}$$

and, for $n \neq 0$, the coefficients $\tilde{F}_n$ are given by

$$\begin{aligned}\tilde{F}_n &= -\mu_0 \frac{2}{L_x} \int_0^{L_x} dx \; e^{-b_0 m_y x} \cos\left(\frac{n\pi x}{L_x}\right) \\ &= -\mu_0 \frac{2b_0 m_y L_x [1 - (-1)^n e^{-b_0 m_y L_x}]}{(b_0^2 m_y^2 L_x^2 + n^2\pi^2)}.\end{aligned} \tag{23}$$

The coefficients $\tilde{D}_n$'s are obtained from Eqs. (21)–(23), and the solutions of $\mu(x, y)$ and $j_y(x, y)$ are given by Eqs. (9)–(11) since all the $\tilde{D}_n$'s are known. We calculate the potential difference $\Delta\mu(L'_y)$, and the total current I_c on the TI surface on the boundary $y = L_y$ using $I_c = \int dx \; j_y(x, y = L_y)$. The formula for I_c is given in Appendix B, see Eq. (B1). From Eq. (B1), we observe that the total current I_c is the same for

both the magnetization directions $m_y = \pm 1$ of the FM and is proportional to μ_0. However, the potential difference $\Delta\mu(L'_y)$, which is given in Appendix B, see Eq. (B2), depends on the FM magnetization direction m_y as well as on μ_0, and $\Delta\mu(L'_y)$ reverses sign if the sign of either μ_0 or the FM magnetization direction m_y is reversed.

If $b_0 L_x = \xi \eta L_x / l_{tr} < 1$, $L_y > L_x$ and $(L_y - L'_y) > L_x$, the terms in the summation for $n \geqslant 1$ can be neglected compared to the first terms in both Eqs. (B1) and (B2), and we obtain

$$I_c \approx 4\sigma' \mu_0 \frac{\sinh^2(b_0 L_x/2)}{b_0^2 L_x^2} c_0 L_x \tanh(c_0 L_y),$$

$$\Delta\mu(L'_y) \approx 4m_y \mu_0 \sinh^2(b_0 L_x/2) \frac{1}{b_0 L_x} \frac{\cosh(c_0 L'_y)}{\cosh(c_0 L_y)}. \tag{24}$$

From Eqs. (17) and (24), we reobtain Eq. (18) which was obtained with the approximation $j_x = 0$ inside the rectangle, previously [43,44]. In the general case, χ is calculated from $\chi = \Delta G/\Delta G^0$, where $\Delta G = \Delta\mu/I_c$ is obtained from Eqs. (B1) and (B2) and ΔG^0 is given in Eq.(19). From Eqs. (B1) and (B2), we observe that both I_c and $\Delta\mu$ becomes zero as $\xi \to 0$, but $\Delta G(\xi \to 0)$ remains finite. We calculate $\Delta G(\xi \to 0)$ from Eqs. (B1) and (B2) using L'Hospital's rule and obtain

$$\begin{aligned}&\Delta G(\xi \to 0) \\ &= \Delta G^0 \left[1 - \frac{8}{\pi^2} \sum_{\substack{n = 2k - 1 \\ k = 1}}^{\infty} \frac{1}{n^2} \frac{\cosh(n\pi L'_y/L_x)}{\cosh(n\pi L_y/L_x)}\right].\end{aligned} \tag{25}$$

From Eq. (25), we observe that $\Delta G(\xi \to 0) \leqslant \Delta G^0$ for the Dirichlet boundary condition.

In Figs. 6(a)–6(d), we show the variation of χ with ξ for different values of L_x/l_{tr} and a given L_y/l_{tr}, L'_y/L_y, and η. The approximate solutions also are plotted in the same figures for comparison. The variation of χ with ξ for the approximate result, i.e., Eq. (18), is independent of L_x but depends on L_y and L'_y. As seen from Figs. 6(a)–6(d), a given L_y/l_{tr}, L'_y, η and ξ, the value of χ from the solution of the Neumann boundary condition decreases with increasing L_x/l_{tr} and deviates from the approximate result with increasing L_x/l_{tr}. It is evident from Figs. 6(a)–6(d) that the validity of the approximate result holds for $b_0 L_x < 1$, $L_y > L_x$ and $(L_y - L'_y) > L_x$. In Figs. 6(e)–6(f), the variation of χ with ξ is shown for different values of L'_y/L_y and a given L_x/l_{tr}, L_y/l_{tr} and η. In Figs. 6(e)–6(f), we also have plotted the result from the solution of Neumann boundary condition (solid line) for comparison along with the approximate result and the result from the Dirichlet boundary condition. It can be seen from Figs. 6(e)–6(f) that the value of χ for the Dirichlet boundary condition deviates more from the approximate one when the conditions $b_0 L_x < 1$, $L_y > L_x$ and $(L_y - L'_y) > L_x$ are not satisfied. Also, we observe from Figs. 6(e)–6(f) that the value of χ for the Dirichlet boundary condition is less than that for
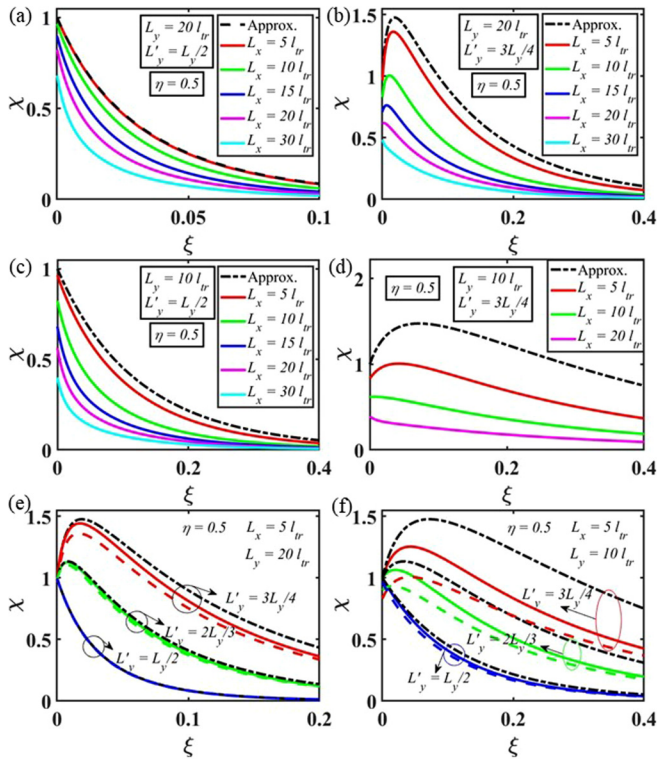
FIG. 6. Variation of χ with ξ calculated for the Dirichlet boundary condition is compared with the approximate result (dotted line): (a)-(c) for different $L_x/l_{tr} = 5, 10, 15, 20, 30$, and (a) $L_y/l_{tr} = 20$, $L_y' = L_y/2$, (b) $L_y/l_{tr} = 20$, $L_y' = 3L_y/4$, (c) $L_y/l_{tr} = 10$, $L_y' = L_y/2$, and (d) for different $L_x/l_{tr} = 5, 10, 20$, $L_y/l_{tr} = 10$, and $L_y' = 3L_y/4$. [(e)–(f)] Results for different $L_y'/L_y = 1/2, 2/3, 3/4$, $L_x/l_{tr} = 5$ and (e) $L_y/l_{tr} = 20$, (f) $L_y/l_{tr} = 10$. The results for the Neumann boundary condition [Figs. 2(e)–(f)] also are shown in (e)–(f) by solid lines. All results are calculated for $\eta = 0.5$.

the Neumann boundary condition given all other parameters remain the same.

We observe that $\chi(\xi \to 0) = \Delta G(\xi \to 0)/\Delta G^0$, which is obtained from Eq. (25), depends on the values of L_x, L_y, and L_y' for the Dirichlet case and complicates the comparison for the behavior of χ vs ξ for different parameter values [as in Fig. 6(f) in which the graphs cross each other]. To make the comparison easier, we have defined $\chi_D = \Delta G/\Delta G(\xi \to 0)$ and show χ_D as a function of ξ in Figs. 7–9 for different values of L_x/l_{tr}, L_y/l_{tr}, L_y', and η.

In Figs. 7(a)–7(d), we show the variation of χ_D with ξ for different values of L_y'/L_y and a given L_x/l_{tr}, L_y/l_{tr} and η. As seen from Figs. 7(a)–7(d), for a given L_x/l_{tr}, L_y/l_{tr}, η and ξ, the value of χ_D increases with increasing L_y'/L_y. In Figs. 8(a)–8(d), the variation of χ_D with ξ is shown for different values of L_y/l_{tr} and a given L_x/l_{tr}, L_y'/l_{tr}, η. It is clear from Figs. 8(a)–8(d) that a given L_x/l_{tr}, L_y'/l_{tr}, η and ξ, the value of χ_D decreases with increasing L_y/l_{tr}. We also have plotted χ instead of χ_D in Figs. 8(e) and 8(f) for the same parameter values as in Fig. 7(a) and Fig. 8(a), respectively. In Fig. 8(e), we show the variation of χ with ξ for different values of L_y'/L_y and a given L_x/l_{tr}, L_y/l_{tr} and η. In Fig. 8(f), the variation of χ with ξ are shown for different values of L_y/l_{tr} and a given L_x/l_{tr}, L_y' and η. However, the change of behavior
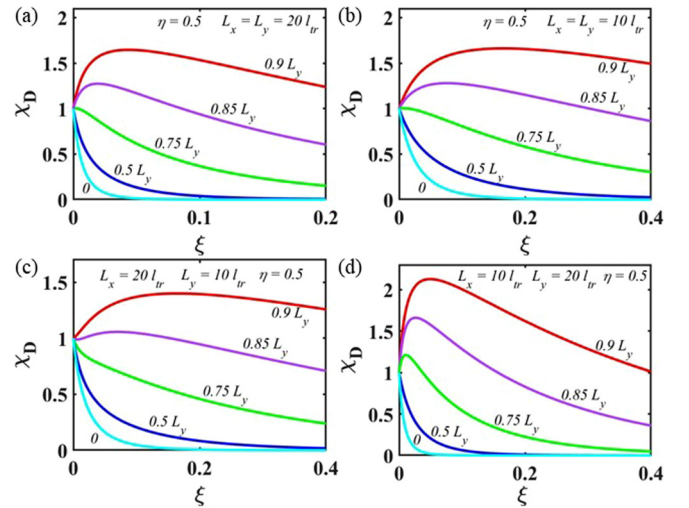

FIG. 7. Variation of χ_D with ξ for different $L_y'/L_y = 0.9, 0.85, 0.75, 0.5, 0$, and (a) $L_x/l_{tr} = L_y/l_{tr} = 20$, (b) $L_x/l_{tr} = L_y/l_{tr} = 10$, (c) $L_x/l_{tr} = 20$, $L_y/l_{tr} = 10$, and (d) $L_x/l_{tr} = 10$, $L_y/l_{tr} = 20$. All results are calculated for $\eta = 0.5$.
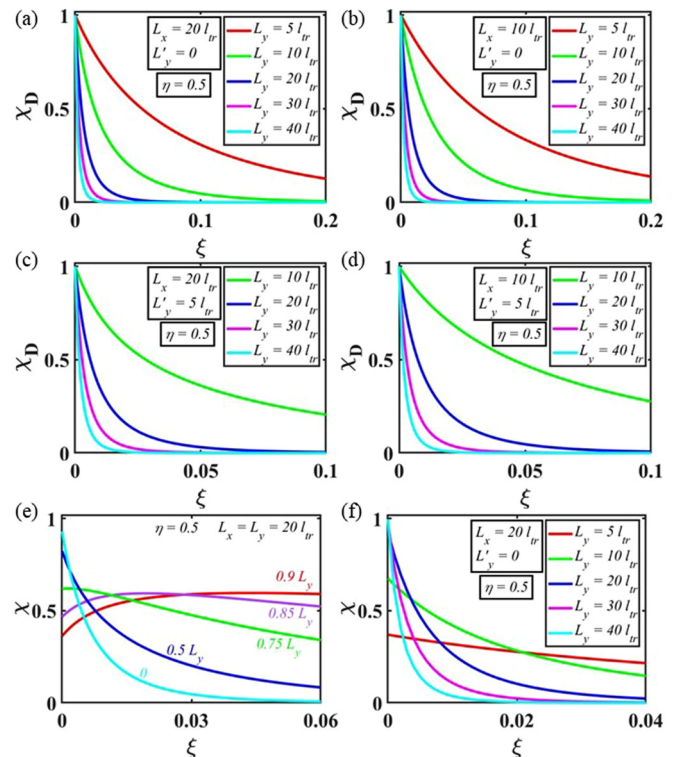

FIG. 8. Variation of χ_D with ξ for different $L_y/l_{tr} = 5, 10, 20, 30, 40$, and (a) $L_x/l_{tr} = 20$, $L_y' = 0$, (b) $L_x/l_{tr} = 10$, $L_y' = 0$, (c) $L_x/l_{tr} = 20$, $L_y'/l_{tr} = 5$, and (d) $L_x/l_{tr} = 10$, $L_y'/l_{tr} = 5$. The results for $L_y = L_y' = 5l_{tr}$ are not shown for (c) and (d). For a comparison of χ_D to χ, variation of χ with ξ is shown in (e) for different $L_y'/L_y = 0.9, 0.85, 0.75, 0.5, 0$ given $L_x/l_{tr} = L_y/l_{tr} = 20$ compared to Fig. 7(a), and in (f) for different $L_y/l_{tr} = 5, 10, 20, 30, 40$ given $L_x/l_{tr} = 20$, $L_y' = 0$ compared to (a) in this figure. All results are calculated for $\eta = 0.5$.
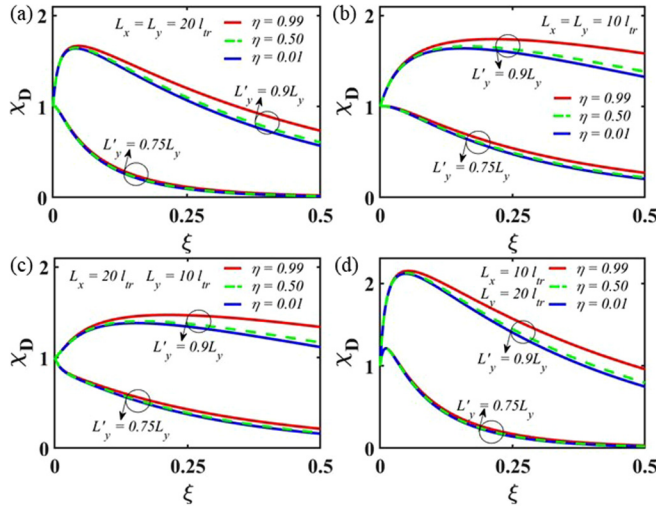
FIG. 9. Variation of χ_D with ξ for different $\eta = 0.99, 0.50, 0.01$ and $L'_y/L_y = 0.9, 0.75$, and (a) $L_x/l_{tr} = L_y/l_{tr} = 20$, (b) $L_x/l_{tr} = L_y/l_{tr} = 10$, (c) $L_x/l_{tr} = 20$, $L_y/l_{tr} = 10$, and (d) $L_x/l_{tr} = 10$, $L_y/l_{tr} = 20$. The results for $\eta = 0.5$ are shown by dotted lines.

of χ with ξ is not monotonic compared to Figs. 7(a) or 8(a). This behavior is because the value of $\chi(\xi \to 0)$ [Eq. (25)] decreases with increasing L'_y a given L_x and L_y as seen in Fig. 8(e), or decreases with increasing L_y a given L_x and L'_y as seen in Fig. 8(f). In Figs. 9(a)–9(d), the variation of χ_D with ξ are shown for different values of η and a given L_x/l_{tr}, L_y/l_{tr}, and L'_y/L_y. Although the value of χ_D slightly decreases with decreasing η, the value of ΔG will almost proportionally decrease with decreasing η, because ΔG is proportional to $\Delta G(\xi \to 0)$ which is proportional to ΔG^0 [Eq. (25)], which is proportional to η [Eq. (19)].

In TI based memory and logic devices in which the FM bit can be switched by passing a charge current on the TI surface in the x-direction as shown in Fig. 1, the FM bit is needed to have the shape anisotropy $L_y > L_x$ [12,29]. The easy axis of the FM bit with $L_y > L_x$ (and the thickness of the FM bit being much smaller than both L_x, L_y) will be along the y direction, which will be orthogonal to the direction of charge current flow on the TI surface, and hence, the easy axis of the FM will be parallel to the direction of the charge current-induced spin polarization vector on the TI surface. The measurement

set-up, as shown in Fig. 1, can be used to read the FM bit with a different read current path than the write current path and without the need of an additional magnetic tunnel junction structure. In these situations with $L_y > L_x$, although the approximate formula for the detected voltage given by Eq. (16) will be valid, a detailed calculation of the two-dimensional transport problem is necessary to model and fitting experimental results. The exact results obtained here quantify the deviations from the prior approximate result which is captured in the variations of the effective parameter χ [Eq. (17)] with different device parameters.

IV. CONCLUSION

In conclusion, we have analyzed the two-dimensional transport on the surface of a topological insulator coupled to a ferromagnet through a tunnel barrier. We have solved the transport equations analytically for two different sets of boundary conditions on the topological insulator surface for the case in which a current is passed from the ferromagnet onto the surface of the topological insulator. The transverse open circuit voltage is calculated which changes in sign upon reversing the ferromagnet magnetization direction. We also calculate the effectiveness of the topological insulator-tunnel barrier-ferromagnet structure in detecting the voltage change upon ferromagnet magnetization reversal, and calculate its behavior with tunneling strength for different dimensions of the device. We show the validity of our approximate result in practical situations such as in TI based memory and logic devices in which the measurement set-up can be used to read and write the FM bit with different read and write paths. A complete analysis of the two-dimensional transport problem presented here will help one to quantify the deviations from the approximate result depending on various device parameters.

APPENDIX A: THE FORMULA FOR $\Delta\mu$ FOR THE NEUMANN BOUNDARY CONDITION

$$\Delta\mu(L'_y) = \frac{4m_y I_c}{\sigma'} \left[\frac{\sinh^2(b_0 L_x/2)}{b_0^2 L_x^2} \frac{b_0 L_x}{c_0 L_x} \frac{\cosh(c_0 L'_y)}{\sinh(c_0 L_y)} + 2 \sum_{\substack{n=2k \\ k=1}}^{\infty} \frac{\sinh^2(b_0 L_x/2)}{(b_0^2 L_x^2 + n^2\pi^2)} \frac{b_0 L_x}{\sqrt{c_0^2 L_x^2 + n^2\pi^2}} \frac{\cosh\left(\sqrt{c_0^2 L_x^2 + n^2\pi^2} L'_y/L_x\right)}{\sinh\left(\sqrt{c_0^2 L_x^2 + n^2\pi^2} L_y/L_x\right)} \right.$$

$$\left. - 2 \sum_{\substack{n=2k-1 \\ k=1}}^{\infty} \frac{\cosh^2(b_0 L_x/2)}{(b_0^2 L_x^2 + n^2\pi^2)} \frac{b_0 L_x}{\sqrt{c_0^2 L_x^2 + n^2\pi^2}} \frac{\cosh\left(\sqrt{c_0^2 L_x^2 + n^2\pi^2} L'_y/L_x\right)}{\sinh\left(\sqrt{c_0^2 L_x^2 + n^2\pi^2} L_y/L_x\right)} \right]. \tag{A1}$$

APPENDIX B: THE FORMULA FOR I_{C} AND $\Delta\mu$ FOR THE DIRICHLET BOUNDARY CONDITION

$$
\begin{aligned}
I_{\mathrm{c}} = 4\sigma'\mu_0 \Bigg[& \frac{\sinh^2(m_y b_0 L_x/2)}{m_y^2 b_0^2 L_x^2} c_0 L_x \tanh(c_0 L_y) + 2\sum_{\substack{n=2k \\ k=1}}^{\infty} \sinh^2(m_y b_0 L_x/2) \\
& \times \left(\frac{m_y b_0 L_x}{m_y^2 b_0^2 L_x^2 + n^2\pi^2}\right)^2 \sqrt{c_0^2 L_x^2 + n^2\pi^2}\, \tanh\left(\sqrt{c_0^2 L_x^2 + n^2\pi^2}\, L_y/L_x\right) \\
& - 2\sum_{\substack{n=2k-1 \\ k=1}}^{\infty} \cosh^2(m_y b_0 L_x/2)\left(\frac{m_y b_0 L_x}{m_y^2 b_0^2 L_x^2 + n^2\pi^2}\right)^2 \sqrt{c_0^2 L_x^2 + n^2\pi^2}\, \tanh\left(\sqrt{c_0^2 L_x^2 + n^2\pi^2}\, L_y/L_x\right) \Bigg],
\end{aligned} \tag{B1}
$$

$$
\begin{aligned}
\Delta\mu(L_y') = 4m_y\mu_0 \Bigg[& \sinh^2(b_0 L_x/2)\frac{1}{b_0 L_x}\frac{\cosh(c_0 L_y')}{\cosh(c_0 L_y)} + 2\sum_{\substack{n=2k \\ k=1}}^{\infty} \sinh^2(b_0 L_x/2)\frac{b_0 L_x}{(b_0^2 L_x^2 + n^2\pi^2)}\frac{\cosh\left(\sqrt{c_0^2 L_x^2 + n^2\pi^2}\, L_y'/L_x\right)}{\cosh\left(\sqrt{c_0^2 L_x^2 + n^2\pi^2}\, L_y/L_x\right)} \\
& - 2\sum_{\substack{n=2k-1 \\ k=1}}^{\infty} \cosh^2(b_0 L_x/2)\frac{b_0 L_x}{(b_0^2 L_x^2 + n^2\pi^2)}\frac{\cosh\left(\sqrt{c_0^2 L_x^2 + n^2\pi^2}\, L_y'/L_x\right)}{\cosh\left(\sqrt{c_0^2 L_x^2 + n^2\pi^2}\, L_y/L_x\right)} \Bigg].
\end{aligned} \tag{B2}
$$

[1] M. Z. Hasan and C. L. Kane, Rev. Mod. Phys. **82**, 3045 (2010).

[2] Y. Ando and M. Shiraishi, J. Phys. Soc. Jpn. **86**, 011001 (2017).

[3] Y. Fan and K. L. Wang, SPIN **06**, 1640001 (2016).

[4] A. Soumyanarayanan, N. Reyren, A. Fert, and C. Panagopoulos, Nature (London) **539**, 509 (2016).

[5] W. Han, Y. Otani, and S. Maekawa, npj Quantum Mater. **3**, 1 (2018).

[6] S. Hong, V. Diep, S. Datta, and Y. P. Chen, Phys. Rev. B **86**, 085131 (2012).

[7] P. Li and I. Appelbaum, Phys. Rev. B **93**, 220404(R) (2016).

[8] T. Yokoyama and Y. Tserkovnyak, Phys. Rev. B **89**, 035408 (2014).

[9] S. Hong, S. Sayed, and S. Datta, Sci. Rep. **6**, 20325 (2016).

[10] S. Sayed, S. Hong, and S. Datta, Sci. Rep. **6**, 35658 (2016).

[11] S. Sayed, S. Hong, and S. Datta, Phys. Rev. Applied **10**, 054044 (2018).

[12] S. Sayed, S. Hong, E. E. Marinero, and S. Datta, IEEE Electron Device Lett. **38**, 1665 (2017).

[13] R. Dey, L. F. Register, and S. K. Banerjee, Phys. Rev. B **100**, 094419 (2019).

[14] C. H. Li, O. M. J. van't Erve, J. T. Robinson, Y. Liu, L. Li, and B. T. Jonker, Nat. Nanotechnol. **9**, 218 (2014).

[15] J. Tang, L.-T. Chang, X. Kou, K. Murata, E. S. Choi, M. Lang, Y. Fan, Y. Jiang, M. Montazeri, W. Jiang, Y. Wang, L. He, and K. L. Wang, Nano Lett. **14**, 5423 (2014).

[16] A. Dankert, J. Geurs, M. V. Kamalakar, S. Charpentier, and S. P. Dash, Nano Lett. **15**, 7976 (2015).

[17] J. S. Lee, A. Richardella, D. R. Hickey, K. A. Mkhoyan, and N. Samarth, Phys. Rev. B **92**, 155312 (2015).

[18] E. K. de Vries, A. M. Kamerbeek, N. Koirala, M. Brahlek, M. Salehi, S. Oh, B. J. van Wees, and T. Banerjee, Phys. Rev. B **92**, 201102(R) (2015).

[19] F. Yang, S. Ghatak, A. A. Taskin, K. Segawa, Y. Ando, M. Shiraishi, Y. Kanai, K. Matsumoto, A. Rosch, and Y. Ando, Phys. Rev. B **94**, 075304 (2016).

[20] A. Dankert, P. Bhaskar, D. Khokhriakov, I. H. Rodrigues, B. Karpiak, M. V. Kamalakar, S. Charpentier, I. Garate, and S. P. Dash, Phys. Rev. B **97**, 125414 (2018).

[21] C. H. Li, O. M. van't Erve, S. Rajput, L. Li, and B. T. Jonker, Nat. Commun. **7**, 13518 (2016).

[22] C. H. Li, O. M. J. van't Erve, Y. Y. Li, L. Li, and B. T. Jonker, Sci. Rep. **6**, 29533 (2016).

[23] C. H. Li, O. M. J. van't Erve, C. Yan, L. Li, and B. T. Jonker, Sci. Rep. **8**, 10265 (2018).

[24] J. Tian, I. Miotkowski, S. Hong, and Y. P. Chen, Sci. Rep. **5**, 14293 (2015).

[25] Y. Ando, T. Hamasaki, T. Kurokawa, K. Ichiba, F. Yang, M. Novak, S. Sasaki, K. Segawa, Y. Ando, and M. Shiraishi, Nano Lett. **14**, 6226 (2014).

[26] S. M. Hus, X.-G. Zhang, G. D. Nguyen, W. Ko, A. P. Baddorf, Y. P. Chen, and A.-P. Li, Phys. Rev. Lett. **119**, 137202 (2017).

[27] A. Leis, M. Schleenvoigt, A. R. Jalil, V. Cherepanov, G. Mussler, D. Grützmacher, F. S. Tautz, and B. Voigtländer, Sci. Rep. **10**, 1 (2020).

[28] J.-h. Lee, H.-j. Kim, J. Chang, S. H. Han, H. C. Koo, S. Sayed, S. Hong, and S. Datta, Sci. Rep. **8**, 1 (2018).

[29] U. Roy, R. Dey, T. Pramanik, B. Ghosh, L. F. Register, and S. K. Banerjee, J. Appl. Phys. **117**, 163906 (2015).

[30] A. Mellnik, J. Lee, A. Richardella, J. Grab, P. Mintun, M. H. Fischer, A. Vaezi, A. Manchon, E.-A. Kim, N. Samarth *et al.*, Nature (London) **511**, 449 (2014).

[31] Y. Wang, P. Deorani, K. Banerjee, N. Koirala, M. Brahlek, S. Oh, and H. Yang, Phys. Rev. Lett. **114**, 257202 (2015).

[32] K. Kondou, R. Yoshimi, A. Tsukazaki, Y. Fukuma, J. Matsuno, K. Takahashi, M. Kawasaki, Y. Tokura, and Y. Otani, Nat. Phys. **12**, 1027 (2016).

[33] Y. Wang, D. Zhu, Y. Wu, Y. Yang, J. Yu, R. Ramaswamy, R. Mishra, S. Shi, M. Elyasi, K.-L. Teo *et al.*, Nat. Commun. **8**, 1 (2017).

[34] S. Shi, A. Wang, Y. Wang, R. Ramaswamy, L. Shen, J. Moon, D. Zhu, J. Yu, S. Oh, Y. Feng, and H. Yang, Phys. Rev. B **97**, 041115(R) (2018).

[35] K. Shen, G. Vignale, and R. Raimondi, Phys. Rev. Lett. **112**, 096601 (2014).

[36] V. Edelstein, Solid State Commun. **73**, 233 (1990).

[37] A. Johansson, J. Henk, and I. Mertig, Phys. Rev. B **93**, 195440 (2016).

[38] L. Liu, A. Richardella, I. Garate, Y. Zhu, N. Samarth, and C.-T. Chen, Phys. Rev. B **91**, 235437 (2015).

[39] W. Luo, W. Y. Deng, H. Geng, M. N. Chen, R. Shen, L. Sheng, and D. Y. Xing, Phys. Rev. B **93**, 115118 (2016).

[40] H. Geng, W. Luo, W. Deng, L. Sheng, R. Shen, and D. Xing, Sci. Rep. **7**, 3755 (2017).

[41] R. Dey, N. Prasad, L. F. Register, and S. K. Banerjee, Phys. Rev. B **97**, 174406 (2018).

[42] W. Chen, J. Phys.: Condens. Matter **32**, 035809 (2019).

[43] R. Dey, L. F. Register, and S. K. Banerjee, Phys. Rev. B **97**, 144417 (2018).

[44] R. Dey, L. F. Register, and S. K. Banerjee, Phys. Rev. B **98**, 219908(E) (2018).

[45] J. B. S. Mendes, O. Alves Santos, J. Holanda, R. P. Loreto, C. I. L. de Araujo, C.-Z. Chang, J. S. Moodera, A. Azevedo, and S. M. Rezende, Phys. Rev. B **96**, 180415(R) (2017).

[46] H. C. Han, Y. S. Chen, M. D. Davydova, P. N. Petrov, P. N. Skirdkov, J. G. Lin, J. C. Wu, J. C. A. Huang, K. A. Zvezdin, and A. K. Zvezdin, Appl. Phys. Lett. **111**, 182411 (2017).

[47] R. Sun, S. Yang, X. Yang, E. Vetter, D. Sun, N. Li, L. Su, Y. Li, Y. Li, Z.-Z. Gong *et al.*, Nano Lett. **19**, 4420 (2019).

[48] J.-C. Rojas-Sánchez, S. Oyarzún, Y. Fu, A. Marty, C. Vergnaud, S. Gambarelli, L. Vila, M. Jamet, Y. Ohtsubo, A. Taleb-Ibrahimi, P. Le Fèvre, F. Bertran, N. Reyren, J.-M. George, and A. Fert, Phys. Rev. Lett. **116**, 096602 (2016).

[49] Y. Shiomi, K. Nomura, Y. Kajiwara, K. Eto, M. Novak, K. Segawa, Y. Ando, and E. Saitoh, Phys. Rev. Lett. **113**, 196601 (2014).

[50] M. Jamali, J. S. Lee, J. S. Jeong, F. Mahfouzi, Y. Lv, Z. Zhao, B. K. Nikolić, K. A. Mkhoyan, N. Samarth, and J.-P. Wang, Nano Lett. **15**, 7126 (2015).

[51] C. N. Wu, Y. H. Lin, Y. T. Fanchiang, H. Y. Hung, H. Y. Lin, P. H. Lin, J. G. Lin, S. F. Lee, M. Hong, and J. Kwo, J. Appl. Phys. **117**, 17D148 (2015).

[52] P. Deorani, J. Son, K. Banerjee, N. Koirala, M. Brahlek, S. Oh, and H. Yang, Phys. Rev. B **90**, 094403 (2014).

[53] F. B. Abdulahad, J.-H. Lin, Y. Liou, W.-K. Chiu, L.-J. Chang, M.-Y. Kao, J.-Z. Liang, D.-S. Hung, and S.-F. Lee, Phys. Rev. B **92**, 241304(R) (2015).

[54] K. T. Yamamoto, Y. Shiomi, K. Segawa, Y. Ando, and E. Saitoh, Phys. Rev. B **94**, 024404 (2016).

[55] J. Kim, C. Jang, X. Wang, J. Paglione, S. Hong, S. Sayed, D. Chun, and D. Kim, Phys. Rev. B **102**, 054410 (2020).